RSC Advances

ROYAL SOCIETY OF CHEMISTRY

www.rsc.org/advances

Graphical contents entry

Excellent room temperature rectification performance and enhanced ferromagnetic phase transition temperature was achieved for the $La_{0.5}Pr_{0.17}Ca_{0.33}MnO_3$ nanofilm/ZnO nanorod *p*-*n* junctions prepared by depositing the $La_{0.5}Pr_{0.17}Ca_{0.33}MnO_3$ shell layer on the ZnO nanorods using the pulsed laser deposition.

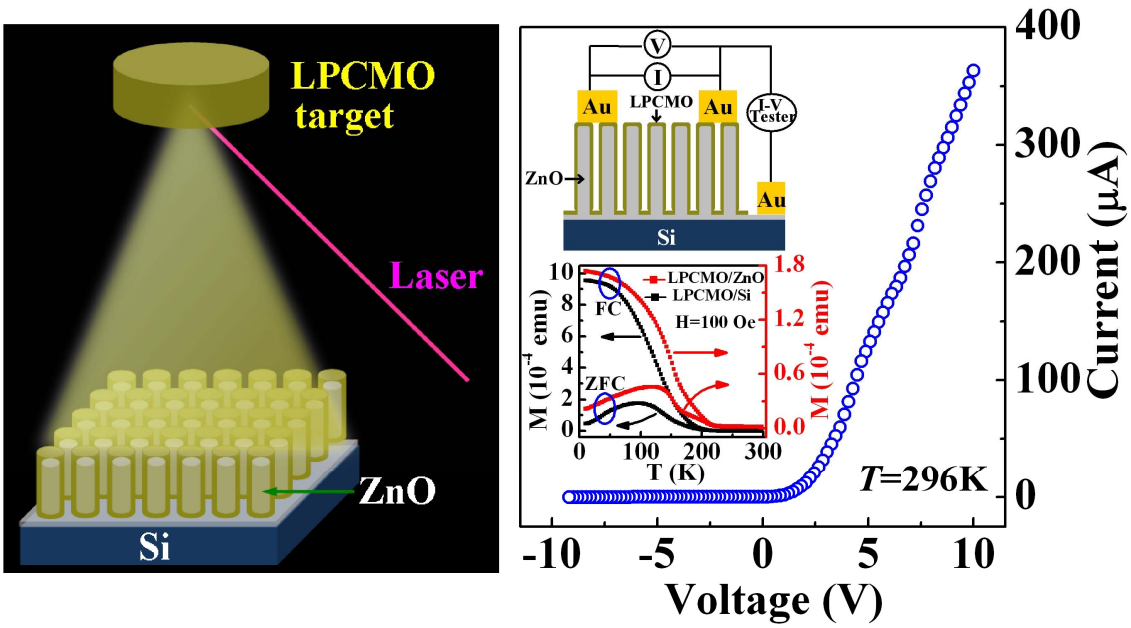

Magnetic and electrical properties of three-dimensional (La,Pr,Ca)MnO_3 nanofilm/ZnO nanorod *p-n* junctions

Ming Zheng, Qiu-Xiang Zhu, Xue-Yan Li, Xiao-Min Li, and Ren-Kui Zheng [a)]

State Key Laboratory of High Performance Ceramics and Superfine Microstructure, Shanghai Institute of Ceramics, Chinese Academy of Sciences, Shanghai 200050, China

Abstract

Three-dimensional (3D) nanostructured *p-n* junctions have been fabricated by growing *p*-type $La_{0.5}Pr_{0.17}Ca_{0.33}MnO_3$ (LPCMO) manganite thin film on *n*-type ZnO nanorod arrays using pulsed laser deposition. The 3D LPCMO nanofilm/ZnO nanorod *p-n* junctions exhibit excellent room temperature rectification performance with a high rectification factor of ~1650 at ±5.0 V, approximately 14 times larger than that of manganite film- and ZnO nanowires (or film)-based layered *p-n* junctions. The ferromagnetic phase transition temperature T_C for the LPCMO nanofilm is significantly (~28 K) higher than that of 2D LPCMO films directly grown on Si substrates, which is interpreted in terms of nanograin-induced surface effect and lattice strain effect. The large portion of magnetically frozen phase establishes the existence of strong electronic phase separation in the 3D nanofilm.

a) *E-mail*: zrk@ustc.edu

Introduction

Hybrid ferromagnet/semiconductor heterostructures for spintronics applications are currently being extensively investigated for the understanding of the electron transport processes across the ferromagnet/semiconductor interfaces.[1] ZnO is a versatile electron-doped semiconductor material with a direct wide band gap of 3.37 eV and a large exciton binding energy of 60 meV, making it promising for various potential applications in electronic devices whose performance was found to be closely associated with the size, morphology and dimensions of the materials.[2] ZnO nanostructures with the wide range of morphological diversity have been reported to exhibit superior physical properties because of the high surface-to-volume ratio. Comparatively, perovskite manganite $La_{1-x-y}Pr_yCa_xMnO_3$ is a hole-doped material that shows a variety of attractive physical phenomena such as the colossal magnetoresistance effect, charge-ordering, electronic phase separation (EPS), and metal-to-insulator phase transition due to the strong interplay among the spin, charge, lattice, and orbital degrees of freedom.[3-6] The ferromagnetic metallic (FMM) phase and the charge-ordered antiferromagnetic insulating (CO/AFI) phase coexist in nanoscale at low temperatures for the $La_{1-x-y}Pr_yCa_xMnO_3$ bulk and films.[3-6] Much efforts have been devoted to understanding the electronic transport and magnetic properties of $La_{1-x-y}Pr_yCa_xMnO_3$ nanostructures including nanoparticles, nanoboxes, and core-shell nanowires in order to fabricate various nanoscale spin-sensitive magnetic devices. For example, Bingham *et al.*[7] and Zhang *et al.*[8] observed a suppression of the CO/AFM phase and a stabilization of the FMM phase with

reducing particle size for $La_{1-x-y}Pr_yCa_xMnO_3$ nanoparticles. Nguyen *et al.*[9] observed enhanced metal-to-insulator transition for the $La_{0.275}Pr_{0.35}Ca_{0.375}MnO_3$ nanoboxes. Li *et al.*[10] reported strong EPS in the single-crystalline $La_{0.33}Pr_{0.34}Ca_{0.33}MnO_3$/MgO core-shell nanowires with a larger magnetic coercivity than that of the corresponding bulk sample. Although the properties of ZnO and $La_{1-x-y}Pr_yCa_xMnO_3$ nanostructures have been investigate, respectively, very little efforts have been made to integrate the *p*-type $La_{1-x-y}Pr_yCa_xMnO_3$ thin film on the *n*-type ZnO nanorods/nanowires and explore the physical properties (especially the rectification behavior) of the nanostructured three-dimensional (3D) $La_{1-x-y}Pr_yCa_xMnO_3$/ZnO *p-n* junctions which may show superior rectification behavior.

In this work, we have fabricated 3D $La_{0.5}Pr_{0.17}Ca_{0.33}MnO_3$(LPCMO) nanofilm/ZnO nanorod *p-n* junctions by growing the LPCMO film on vertically aligned ZnO nanorod arrays that was prepared by the polyethylenimine-assisted hydrothermal method, and found excellent room temperature rectifying behavior with a high rectification factor ~1650 for the junctions. Due to the nanograin-induced surface effect and lattice strain effect, the 3D LPCMO nanofilm shows significantly enhanced Curie temperature, as compared with that of the 2D LPCMO film. Moreover, a large amount of magnetically frozen phase and a magnetoresistance (*MR*) value of 68% were observed for the LPCMO nanofilm/ZnO nanorod *p-n* junctions. These electrical and magnetic properties are associated with the structure and morphology of the 3D nanofilm.

Experimental

120 nm thick ZnO seed-layer film were firstly grown on HF-cleaned high resistive Si(100) substrates by the sol–gel dip-coating method.[11] ZnO nanorod arrays were then grown on the ZnO film-seeded Si(100) substrates via the polyethylenimine (PEI)-assisted hydrothermal method (PAHT) using precursor aqueous solutions of zinc nitrate hexahydrate ($Zn(NO_3)_2 \cdot 6H_2O$) and hexamethylenetetramine (HMT), as reported previously.[11] LPCMO films were simultaneously deposited onto the as-prepared ZnO nanorod arrays and HF-cleaned Si(100) substrates by pulsed laser deposition at a substrate temperature of 700 ^oC and an oxygen pressure of 27 Pa. Both the LPCMO thin films on ZnO nanorods and Si substrates were *in situ* annealed at 1 atm O_2 for 30 mins to increase the crystallinity and reduce oxygen deficiencies in the LPCMO films. Here, the LPCMO thin films directly grown on the HF-cleaned Si(100) substrates were used as the "reference sample" for comparison purposes.

The morphology, structure, and chemical compositions of the samples were investigated using field emission scanning electron microscope (FESEM, Magellan 400) and high resolution transmission electron microscope (HRTEM, Tecnai G2 F20) attached with an energy-dispersive x-ray spectrometer (EDS). The phase purity was examined by a high resolution Bruker D8 Discover (Cu $K_{\alpha 1}$ radiation, λ=1.5406 Å) X-ray diffractometer (XRD). Magnetic data were collected using a SQUID magnetometer (MPMS XL-5, Quantum Design) with the magnetic field applied parallel and perpendicular to the plane of Si substrates, respectively. The top and bottom gold electrodes were sputtered onto the LPCMO nanofilm and the ZnO seed layer film for electrical transport measurements. The schematic of the experimental

setup is illustrated in the inset (a) of Fig. 6. The resistance of the LPCMO nanofilm between the two top-top Au electrodes was measured with a physical property measurement system (PPMS-9, Quantum Design). The current-voltage (*I*-*V*) characteristics of the LPCMO nanofilm/ZnO nanorod *p*-*n* junctions were analyzed using a Precision Multiferroic Analyzer (Radiant Technologies. Inc. USA) through the top and bottom Au electrodes.

Results and discussion

As can be seen in Fig. 1(a), vertically-aligned ZnO nanorods have been successfully grown on the ZnO film-seeded Si substrate and exhibit diameters of 100-200 nm and lengths of 400-500 nm (cross-sectional SEM image is not shown here) with a smooth hexagonal top surface [see the inset of Fig. 1(a)], suggesting that the ZnO nanorods grow preferentially along the (0001) crystal direction. The morphologies of the 3D LPCMO nanofilm on the ZnO nanorods are displayed in Figs. 1(c) and 1(d), where the length of the nanorods increases from 400-500 to 700-800 nm with a higher density due to the growth of the LPCMO film on the ZnO nanorods. The immediate sputtering deposition of the LPCMO film on the ZnO nanorods leads to the change in the morphology from sharply flat tip for the pristine ZnO nanorods to dull tip for the final LPCMO/ZnO nanostructure, as can be seen in the inset of Fig. 1(c). In contrast, columnar grains were observed for the 2D reference sample which was directly deposited on the Si(100) substrates [Fig. 1(f)]. The lower panel of Fig. 1(e) shows the XRD pattern of the 2D reference sample directly grown on the Si substrates. LPCMO (112) [also see the expand view shown in the inset of

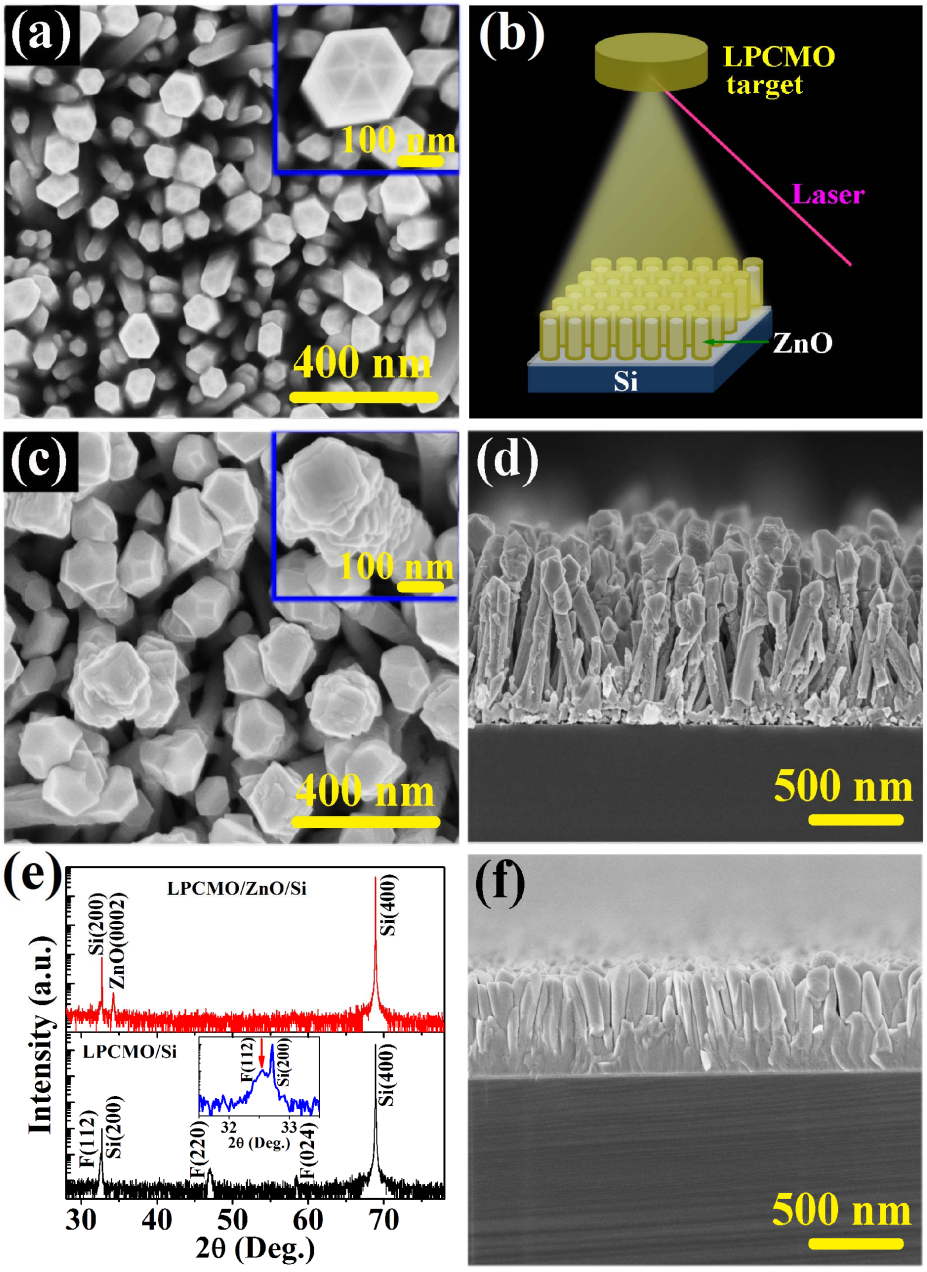

Fig. 1 (a) Top view SEM image of the ZnO nanorods. Inset: enlarged top view of a nanorod. (b) Schematic illustration of PLD deposition of the LPCMO film on the ZnO nanorods. (c) Top view SEM image of the LPCMO/ZnO nanostructure. Inset: enlarged top view of the LPCMO/ZnO nanostructure. (d) Cross-sectional SEM image of the LPCMO/ZnO nanostructure. (e) XRD patterns of the LPCMO film grown on the ZnO nanorods (upper panel) and the Si substrate (lower panel). Inset: expanded view near Si(200) diffraction peak, "F" represents the LPCMO film. (f) Cross-sectional SEM image of the LPCMO film directly grown on the Si substrate.

Fig. 1(e)], (220) and (024) diffraction peaks appear, confirming the polycrystalline pseudo-cubic crystal structure of the reference sample, presumably caused by the large lattice mismatch (~29%) between the LPCMO and the Si substrate. The XRD pattern shown in the upper panel of Fig. 1(e) indicates that the ZnO nanorods are indeed (0001) preferentially oriented, which is consistent with the SEM observation. Due to the polycrystalline nature and very small amount of the LPCMO film grown on the ZnO nanorods, no diffraction peak from the LPCMO film can be detected by XRD. However, TEM, EDS, electrical transport, and magnetic results indeed showed that the LPCMO film had been deposited on the ZnO nanorods and will be discussed in the following paragraphs.

Fig. 2(a) shows a TEM image taken on a typical LPCMO/ZnO core-shell heterostructure, which indicates that the average thickness of the LPCMO film on the

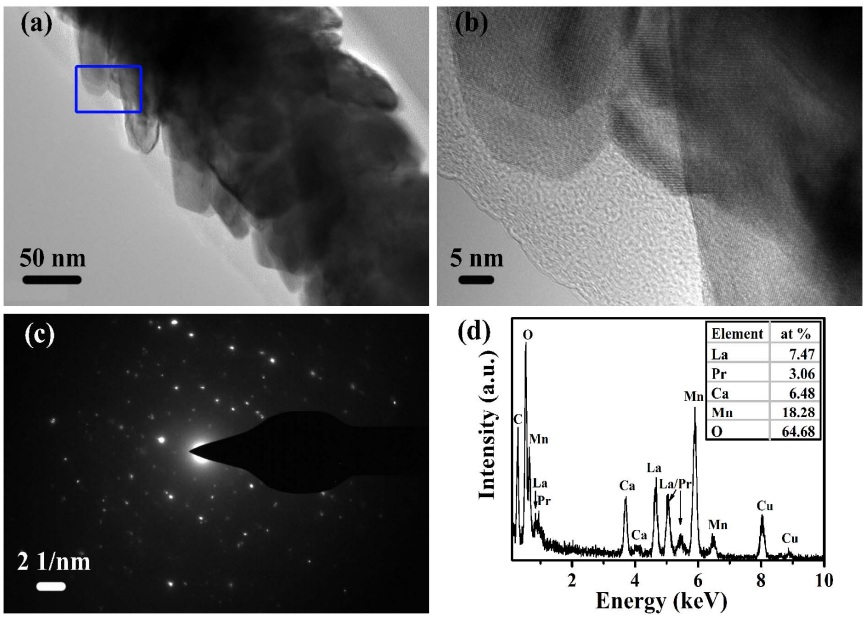

Fig. 2 (a) TEM image of a LPCMO/ZnO core-shell nanorod. (b) HRTEM image taken from the highlighted area in (a). (c) SAED pattern of the LPCMO nanofilm on a ZnO nanorod. (d) Corresponding EDS spectrum.

ZnO nanorods is ~40 nm, much thinner than that of the reference sample (~550 nm). This could probably be attributed to the much larger surface area of the ZnO nanorods than that of the Si substrate. The HRTEM image [Fig. 2(b)] clearly displays the lattice structure of the LPCMO nanofilm on the ZnO nanorods with atomic resolution. The corresponding selected area electron diffraction (SAED) [Fig. 2(c)] also reveals the polycrystalline nature of the LPCMO nanofilm. The EDS spectrum of the LPCMO nanofilm is shown in Fig. 2(d), where the quantified contents of La, Pr, Ca, Mn, and O are approximately 7.47 at %, 3.06 at %, 6.48 at %, 18.28 at %, and 64.68 at %, respectively. The chemical compositions of the LPCMO nanofilm are similar to those of the stoichiometric LPCMO ceramic target. We note that EDS measurements taken on the LPCMO nanofilm did not detect any Zn element, indicating no interfacial diffusion and reaction between the outer LPCMO nanofilm and the inner ZnO nanorods. Altogether, the above results establish the good quality of the nanostructured LPCMO nanofilm/ZnO nanorod heterostructure.

Fig. 3 shows the temperature (T) dependence of the zero-field-cooled (ZFC) and field-cooled (FC) magnetization (M) for the LPCMO/ZnO heterostructure and the reference sample, as measured with the magnetic field applied parallel to the plane of the Si substrates. Similar to the findings for $La_{1-x-y}Pr_yCa_xMnO_3$ bulk and films,[12,13] a pronounced magnetic irreversibility was observed below T_{IR} where the FC M versus T curve deviates from the ZFC one for the LPCMO/ZnO heterostructure and moreover, a broad peak in the ZFC M versus T curve was observed at T_{CG} ~118 and 94 K (as measured at H=100 Oe) for the LPCMO/ZnO and the reference sample,

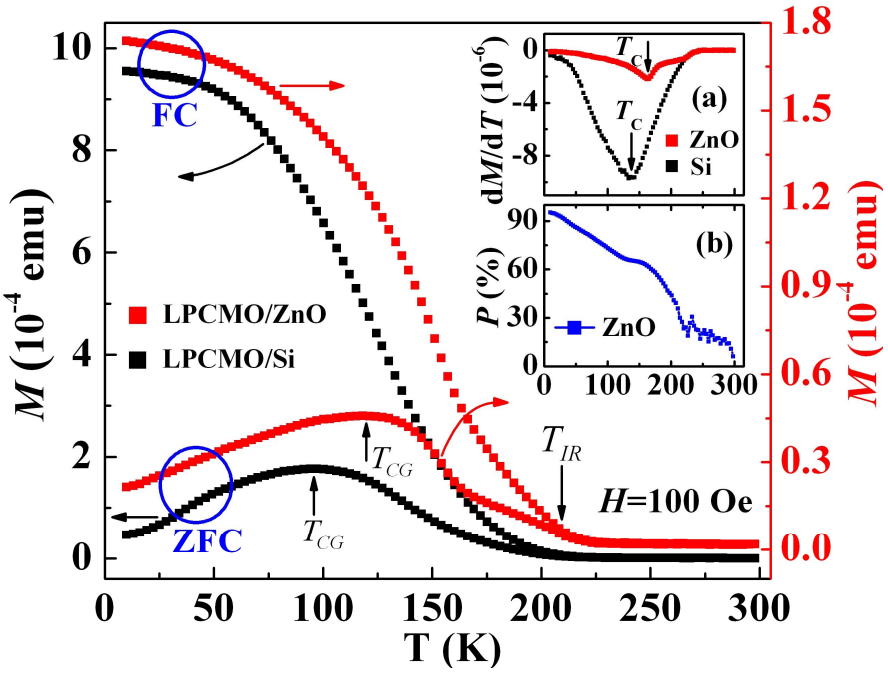

Fig. 3 Temperature dependence of ZFC and FC magnetization for the LPCMO/ZnO nanostructure and the LPCMO/Si sample. Insets (a): $dM/dT \sim T$ curves for the LPCMO/ZnO nanostructure and the LPCMO/Si sample, respectively. Inset (b): temperature dependence of the frozen phase concentration P for the LPCMO/ZnO nanostructure.

respectively, which is a typical magnetic cluster-glass behavior due to the frozen of the magnetic moments below T_{CG}.[12,13] Note that very similar magnetic behavior has been observed in the $La_{0.9}Ca_{0.1}MnO_3$ nanocrystals where nanometer sized ferromagnetic clusters embedded in the canted antiferromagnetic matrix.[14] At low temperatures ($T<T_{CG}$), the $La_{1-x-y}Pr_yCa_xMnO_3$ is frozen in a metastable configuration with a certain fraction of FMM phase distributed as isolated clusters surrounded by the majority CO/AFI matrix.[15] As can be seen in the inset (b) Fig. 3, the difference between the ZFC magnetic moment to the FC magnetic moment, defined as the frozen phase magnetic moment,[10] increases significantly below T_{IR} (~210 K),

indicating that the EPS develops below T_{IR}. A large frozen phase concentration P, $P=[M(FC)-M(ZFC)]/M(FC)$,[10] of ~88%, was observed for the LPCMO nanofilm/ZnO nanorods heterostructure, which is a result of the strong electronic phase separation in the 3D LPCMO nanofilm.

It is worth noting that the paramagnetic-to-ferromagnetic phase transition temperature T_C, derived from the field-cooled dM/dT versus T curve (see the inset (a) of Fig. 3) of the LPCMO nanofilm/ZnO nanorod heterostructure (~164 K) is significantly higher than that of the reference sample (~133 K). Such large increase in T_C (ΔT_C~28 K) is probably associated with the LPCMO particle size reduction-induced surface effect and lattice strain effect. For the 3D LPCMO nanofilm grown on the ZnO nanorods, the grain size is much smaller than that of the 2D LPCMO film directly grown on the Si substrates and moreover, the surface area of the former is clearly much larger than that of the latter, resulting in a much larger surface-to-volume ratio for the former. As a consequence, there is a large amount of uncompensated surface spins for the LPCMO nanofilm, which would weaken the antiferromagnetic interaction and favors the formation of ferromagnetic clusters.[8,16] Furthermore, some of the ferromagnetic clusters near the surface may find percolation paths through the antiferromagnetic matrix, favoring long range FM spin ordering.[8] Moreover, the tunneling of charge carriers between two Mn ions which belong to different adjacent grains also induces ferromagnetic double exchange correlation.[14] In addition, it was found that, associated with the reduction in particle size of doped manganites, two pronounced lattice effects (i.e., a contraction of the

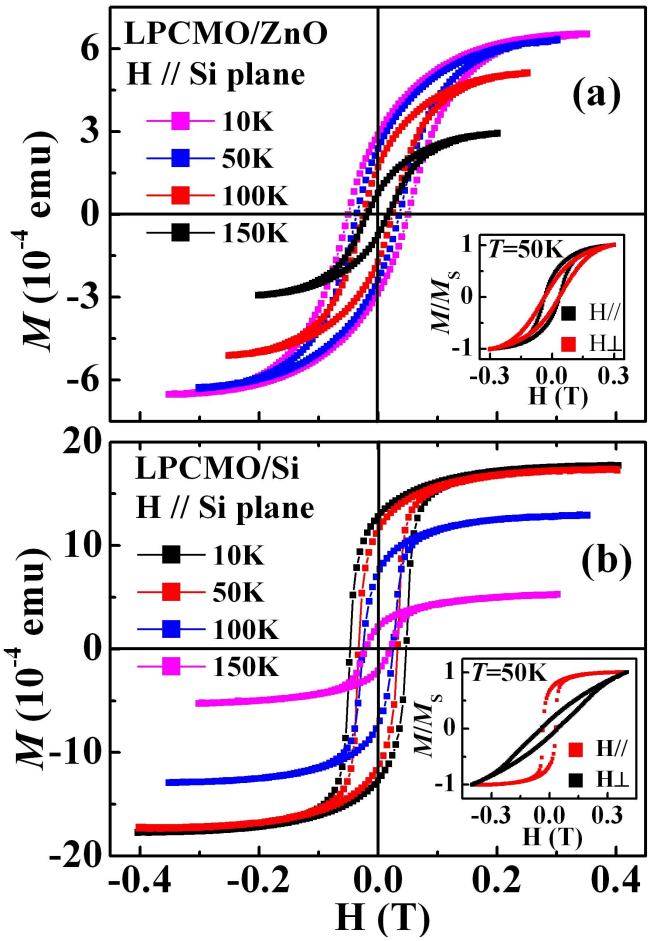

Fig. 4. Magnetization-magnetic field (M-H) hysteresis loops of (a) LPCMO/ZnO and (b) LPCMO/Si at temperatures as stated. Insets in (a) and (b) show the corresponding M-H hysteresis loops at T=50 K, with the magnetic field applied parallel and perpendicular to the plane of the Si substrates, respectively.

unit cell volume and a reduction of the unit cell anisotropy) would cause a decrease in the Mn-O bond length and an increase in the Mn-O-Mn bond angle and thus enhances the electronic bandwidth,[17-19] thereby favoring active hopping of charge carriers. According to the double-exchange model,[20] enhanced active hopping of charge carriers would induce stronger ferromagnetic coupling between neighboring Mn ions, giving rise to higher T_C. Therefore, it is believed that the nanograin-induced surface effect and lattice strain effect are responsible for the enhanced T_C for the

LPCMO/ZnO structure. Below T_C, both samples show a considerable enhancement of ferromagnetic behavior with decreasing temperature, as manifested by well-defined magnetic hysteresis (*M*-*H*) loops and a remarkable increase in the area of the loops from *T*=150 to 10 K [see Fig. 4(a) and 4(b)]. The inset of Fig. 4(b) shows the M/M_S as a function of *H* at *T*=50 K for the reference sample, as measured with the magnetic field applied parallel and perpendicular to the plane of the Si substrates, respectively. One can see that the in-plane magnetization is significantly enhanced compared with the out-of-plane counterpart, implying the presence of anisotropic demagnetization effect.[21] On the contrary, an isotropic magnetization behavior of the LPCMO/ZnO heterostructure was observed, as reflected by the similar in-plane and out-of-plane magnetization [inset of Fig. 4(a)]. Obviously, the exotic magnetic isotropy behavior is dependent on the structure and morphology of the 3D nanostructured LPCMO film.[22,23]

The growth-determined morphology does not only have a considerable impact on the magnetic properties but also strongly influences the electronic transport of the LPCMO nanofilm. The inset of Fig. 5(a) shows the temperature dependence of the resistance under various magnetic fields for the reference sample which undergoes an insulator-to-metal transition at T_{MIT} =146 K for *H*=0 T. In contrast, the LPCMO nanofilm on the ZnO nanorods shows a typical semiconductor-like electrical behavior with a charge-ordering phase transition at T_{CO}=56 K even under *H*=9 T, where the resistance shows an upturn. At *T*=10 K, it is roughly estimated that the resistance of the LPCMO/ZnO structure is two orders of magnitude larger than that

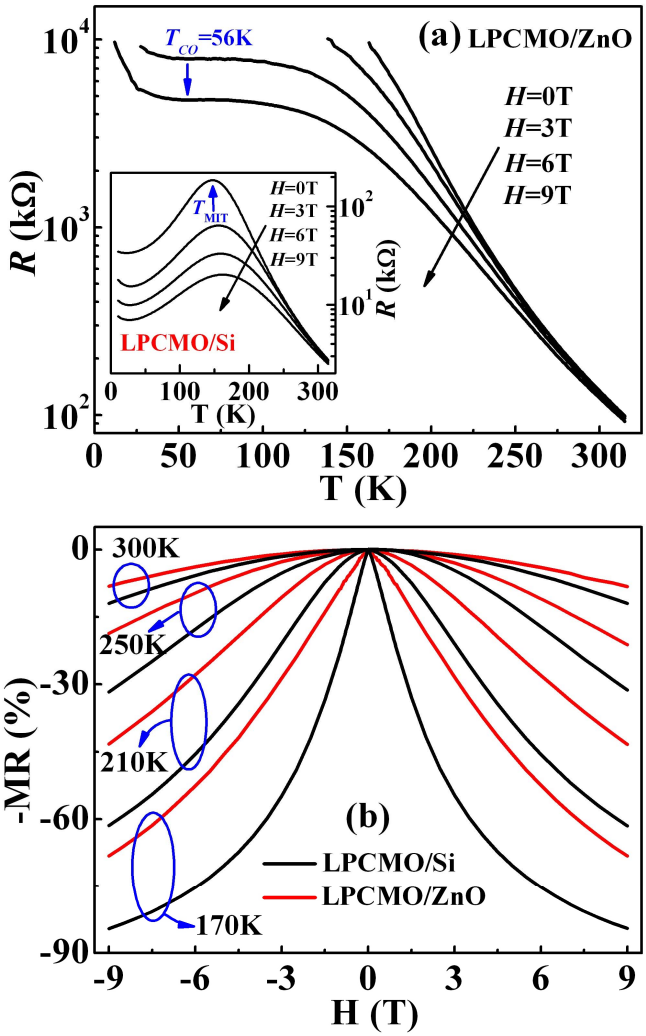

Fig. 5 (a) Temperature dependence of the resistance at *H*=0, 3, 6 and 9 T for the LPCMO/ZnO nanostructure. Inset: temperature dependence of the resistance at *H*=0, 3, 6 and 9 T for the LPCMO/Si sample. (b) MR versus *H* curves for the LPCMO/ZnO nanostructure and the LPCMO/Si sample at temperatures as stated.

of the reference sample. For the 3D LPCMO/ZnO heterostructure, there exists a large amount of nanograins through which charge carriers cross or tunnel,[24] which would obviously cause a larger resistance for the LPCMO/ZnO heterostructure. Moreover, nanograin-induced spin disorder at grain surface also contributes to the high resistance of the LPCMO nanofilm.[25] A magnetic field can easily align these disordered spins and thus reduces the scattering process of the charge carriers,

thereby causing MR effect. MR of the LPCMO/ZnO heterostructure was measured as a function of *H* at various temperatures and the results are shown in Fig. 5(b). For comparison, the *MR* versus *H* curves for the reference samples are also shown in Fig. 5(b). At a fixed temperature (e.g., *T*=170 or 300 K), M*R* of the LPCMO/ZnO heterostructure increases monotonously with increasing *H* and no saturation was observed. Nevertheless, at any fixed temperature, MR of the LPCMO/ZnO heterostructure is smaller than that of the reference sample. It is noteworthy that unconventional positive MR effect has been found in the $La_{0.5}Pr_{0.2}Sr_{0.3}MnO_3$ film/ZnO film layered *p-n* junctions and was justified on the basis of magnetic-field-induced enhancement of junction barrier height which is associated with the interface between the $La_{0.5}Pr_{0.2}Sr_{0.3}MnO_3$ film and the ZnO film.[26] It is anticipated that such positive MR effect also exits in the LPCMO nanofilm/ZnO nanorods *p-n* junctions, arising from the interface effect. As a consequence, the inherent negative MR effect of the LPCMO nanofilm will be partly cancelled by the interface-related positive MR effect, leading to the reduced MR effect. Note that similar reduction in the MR effect has been found in the $Pr_{0.5}Ca_{0.5}MnO_3$/ZnO core-shell nanostructure,[27] as compared with that of $Pr_{0.5}Ca_{0.5}MnO_3$ bulk. Aside from this, MR value of ~68% was achieved at *T*=170 K for *H*=9 T for the LPCMO nanofilm/ZnO nanorod heterostructure, which is comparable to that of the $MgO/La_{0.67}Ca_{0.33}MnO_3$ core-shell single-crystal nanowires,[28] suggesting the high quality of the LPCMO nanofilm/ZnO nanorod heterostructure. Such an appreciable MR effect of the 3D LPCMO nanofilm is noteworthy and the interface effect of the

heterostructure are promising to be controlled through growth process for the optimization of the properties.

The current-voltage (*I*-*V*) characteristics of the LPCMO/ZnO *p*-*n* junction are studied and shown in Fig. 6, which shows an evident asymmetric feature under forward and reverse bias conditions. An apparent electrical rectifying behavior was

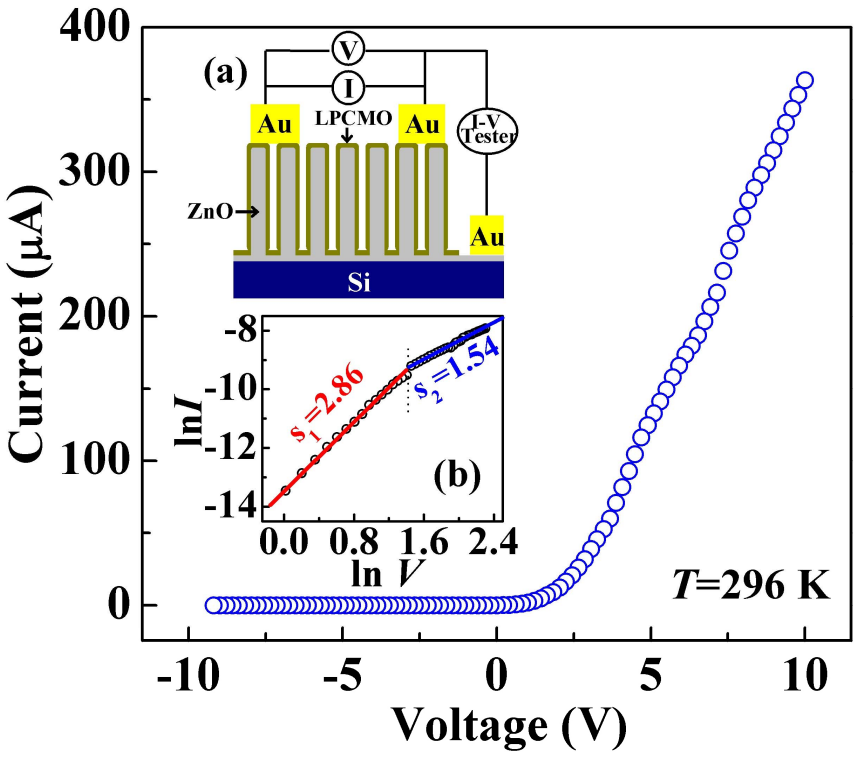

FIG. 6 Current-voltage (*I*-*V*) characteristics of the LPCMO/ZnO nanostructure. Inset (a): schematic experimental setup for measurements of resistance of the LPCMO nanofilm and the *I*-*V* characteristics of the LPCMO/ZnO core-shell nanostructure. Inset (b) ln*I* versus ln*V* curve in the forward region.

observed, revealing the formation of a typical *p*-*n* junction at the interface. This is consistent with the well-known fact that the LPCMO and the ZnO generally display *p*-type and *n*-type conductivity, respectively. The forward turn-on voltage appears at ~1.7 V, and the reverse breakdown voltage is beyond 9 V with a quite low leakage

current of less than 200 nA. The rectification factor (i.e., the forward-to-reverse current ratio) at ±5.0 V reaches 1650, which is approximately 14 times larger than that of manganite film- and ZnO nanowires (or film)-based layered *p*-*n* junctions, e.g., $La_{0.7}Sr_{0.3}MnO_3$ film/ZnO nanowires layered structures,[29-31] demonstrating superior rectifying properties of the present nanostructured LPCMO film/ZnO nanorods *p*-*n* junctions. Such large rectification factor may probably relate to the large fraction of interface area for the LPCMO nanofilm/ZnO nanorods. To further probe into the electric conduction mechanism of the nanostructured LPCMO/ZnO junctions, we showed the ln*I* versus ln*V* curve in the inset (b) of Fig. 6. The curve exhibits two regions with the slope evolving from ~2.86 to ~1.54, which indicates that the leakage mechanism is mainly caused by the space-charge-limited current.[32] The trap sites inside the 3D LPCMO nanofilm and at the interface would capture injected electrons with increasing electric filed, thus degrading the pure space charge effect,[32] as reflected by the fact that the slope is not exactly close to 2. More in-depth work is necessary to gain further detailed information on the conduction mechanisms of the nanostructured LPCMO/ZnO *p*-*n* junctions.

Conclusions

In summary, we have fabricated 3D LPCMO nanofilm/ZnO nanorod *p*-*n* junctions by a two-step process, including the growth of ZnO nanorods using the polyethylenimine-assisted hydrothermal method and the deposition of the LPCMO shell layer on the ZnO nanorods using PLD. Such fabricated *p*-*n* junctions show outstanding room temperature rectification performance with a rectification factor of

~1650 at ±5.0 V, approximately 14 times larger than that of manganite film- and ZnO nanowires (or film)-based layered *p*-*n* junctions. The 3D LPCMO nanofilm shows a higher Curie temperature (ΔT_C ~28 K) than that of the 2D reference sample, which is interpreted in terms of the nanograin-induced surface effect and lattice strain effect. The large portion of the magnetically frozen phase demonstrates the existence of strong EPS in the 3D nanofilm. Our findings provide an approach to integrate perovskite manganite and ZnO in 3D nanostructure with designed morphology and physical properties for building advanced nanoscale electronic and magnetic devices.

Acknowledgements

This work was supported by the NSFC (Grant Nos. 51172259, 11090332) and the CAS/SAFEA International Partnership Program for Creative Research Teams.

References

[1] T. Taniyama, E. Wada, M. Itoh, and M. Yamaguchi, *NPG Asia Mater.*, 2011, **3**, 65.

[2] U. Ozgur, Y. I. Alivov, C. Liu, A. Teke, M. A. Reshchikov, S. Dogan, V. Avrutin, S. J. Cho, and H. Morkoc, *J. Appl. Phys.*, 2005, **98**, 041301.

[3] M. Uehara, S. Mori, C. H. Chen, and S. W. Cheong. *Nature*, 1999, **399**, 560.

[4] L. W. Zhang, C. Israel, A. Biswas, R. L. Greene, and A. de Lozanne, *Science*, 2002, **298**, 805.

[5] T. Z. Ward, S. Liang, K. Fuchigami, L. F. Yin, E. Dagotto, E. W. Plummer, and J. Shen, *Phys. Rev. Lett.*, 2008, **100**, 247204.

[6] T. Z.Ward, J. D. Budai1, Z. Gai1,2, J. Z. Tischler1, Lifeng Yin1 and J. Shen, *Nat. Phys.*, 2009, **5**, 885.

[7] N. S. Bingham, P. Lampen, M. H. Phan, T. D. Hoang, H. D. Chinh, C. L. Zhang, S. W. Cheong, and H. Srikanth, *Phys. Rev. B*, 2012, **86**, 064420.

[8] T. Zhang and M. Dressel, *Phys. Rev. B*, 2007, **80**, 014435.

[9] T. V. A. Nguyen, A. N. Hattori,Y. Fujiwara, S. Ueda, and H. Tanaka, *Appl. Phys. Lett*., 2013, **103**, 223105.

[10] L. Li, H. Li, X. F. Zhai, and C. G. Zeng, *Appl. Phys. Lett*., 2013, **103**, 113101.

[11] J. J. Qiu, X. M. Li, F. W. Zhuge, X. Y. Gan, X. D. Gao, W. Z. He, S. J. Park, H. K. Kim, and Y. H. Hwang, *Nanotechnology*, 2010, **21**, 195602.

[12] H. Jeen and A. Biswas, *Phys. Rev. B*, 2011, **83**, 064408.

[13] M. Zheng, X. Y. Li, M. M. Yang, Q. X. Zhu, Y. Wang, X. M. Li, X. Shi, H. L. W. Chan, X. G. Li, H. S. Luo, and R. K. Zheng, *Appl. Phys. Lett.*, 2013, **103**, 263507.

[14] E. E. Rozenberg, A. I. Shames, M. Auslender, G. Jung, I. Felner, Jaivardhan Sinha, S. S. Banerjee, D. Mogilyansky, E. Sominski, A. Gedanken, Ya. M. Mukovskii, and G. Gorodetsky, *Phys. Rev. B*, 2007, **76**, 214429.

[15] L. Ghivelder and F. Parisi, *Phys. Rev. B*, 2005, **71**, 184425.

[16] T. Zhang, T. F. Zhou, T. Qian, and X. G. Li, *Phys. Rev. B*, 2007, **76**, 174415.

[17] A. Dutta, N. Gayathri, and R. Ranganathan, *Phys. Rev. B*, 2003, **68**, 054432.

[18] T. Sarkar, P. K. Mukhopadhyay, and A. K. Raychaudhuri, *J. Appl. Phys*., 2007, **101**, 124307.

[19] K. S. Shankar, S. Kar, G. N. Subbanna, A. K. Raychaudhur, *Solid State Commun*., 2004, **129**, 479.

[20] C. Zener, *Phys. Rev*., 1951, **82**, 403.

[21] M. Jain, Y. Li, M. F. Hundley, M. Hawley, B. Maiorov, I. H. Campbell, L. Civale, and Q. X. Jia, *Appl. Phys. Lett*., 2006, **88**, 232510.

[22] H. Y. Gao, M. Staruch, M. Jain, P. X. Gao, P. Shimpi, Y. B. Guo, W. J. Cai, and H. J. Lin, *Appl. Phys. Lett*., 2011, **98**, 123105.

[23] M. Mathews, F. M. Postma, J. C. Lodder, R. Jansen, G. Rijnders, and D. H. A. Blank, *Appl. Phys. Lett*., 2005, **87**, 242507.

[24] H. Y. Hwang, S. W. Cheong, N. P. Ong, and B. Batlogg, *Phys. Rev. Lett.* **77**, 2041 (1996).

[25] M. H. Zhu, Y. G. Zhao, W. Cai, X. S. Wu, S. N. Gao, K. Wang, L. B. Luo, H. S. Huang, and L. Lu, *Phys. Rev. B* **75**, 134424 (2007).

[26] U. D. Khachar, P. S. Solanki, R. J. Choudhary, D. M. Phase, V. Ganesan, and D. G. Kuberkar, *Appl. Phys. A*, 2012, **108**, 733.

[27] R. V. K. Mangalam, Z. Zhang, T. Wu, and W. Prellier, *Appl. Phys. Lett.*, 2011, **99**, 103102.

[28] S. Han, C. Li, Z. Q. Liu, B. Lei, D. H. Zhang, W. Jin, X. L. Liu, T. Tang, and C. W. Zhou, *Nano Lett*., 2004, **4**, 1241.

[29] Z. Zhang, Y. H. Sun, Y. G. Zhao, G. P. Li, and T. Wu, *Appl. Phys. Lett.*, 2008, **92**, 103113.

[30] A. Tiwari, C. Jin, D. Kumar, and J. Narayan, *Appl. Phys. Lett.*, 2003, **83**, 1773.

[31] Y. C. Liang, C. Y. Hu, H. Zhong, J. L. Wang, *Nanoscale*, 2013, **5**, 2346.

[32] X. Q. Zhao W. Wang, C. Zheng, Q. X. Zhu, X. M. Li, R. K. Zheng, *J. Mater. Sci.: Mater. Electron.*, 2013, **24**, 1677.